Chapter 1

Introduction

The solar corona is the tenuous outer atmosphere of the Sun which is revealed to the human eye during a total solar eclipse, or with space observations. The visible spectrum of the solar corona has two major components: a continuum (the K-corona), due to Thomson scattering of photospheric light by the free electrons in the corona; and weak absorption lines (corresponding to the Fraunhofer lines - the F-corona), superimposed on a continuum emission. The latter is due to scattering by interplanetary dust particles in the immediate vicinity of the Sun. In addition, emission lines of highly-ionised atoms (e.g. the green coronal line Fe XIV 5303 Å and the red Fe X 6374 Å) are also observed. Their visibility clearly indicates the presence of million-degree plasma in the solar corona. From white light coronagraph observations, and using a model for the distribution of electrons in the corona following *van de Hulst* (1950), it is possible to estimate the electron density, which has values of the order of 10^8 cm^{-3}. Hence, even before the advent of space-based observations, ground-based data had revealed that the solar corona is mainly composed of high-temperature and low-density plasma. Due to its characteristics, this plasma is mostly optically thin and emits principally in X-rays and in the Extreme Ultra-Violet (EUV, 100-900 Å) region of the spectrum, and detailed studies therefore require observations from space.

For a general introduction to the Sun and the solar atmosphere, see, e.g.: *Athay* (1976); *Phillips* (1992); *Mariska* (1992); *Golub and Pasachoff* (1997).

The solar corona has been studied in more detail since the early 1960s using data from a number of rocket flights. Detailed studies started with Skylab, which observed the solar corona with various instruments from June 1973 to February 1974. Skylab's data together with a number of rocket flights and Yohkoh observations, have been the main observational source of information for our understanding of the solar corona, until 1996. In December 1995, the NASA/ESA Solar and Heliospheric Observatory (SOHO), one of the four major cornerstones of the ESA's Horizon 2000 project, was launched successfully.

It makes continuous observations of the Sun using 12 complementary instruments that allow for the first time a wide range of simultaneous observations at different wavelengths. It has greatly extended the limited information on the solar corona that was previously available.

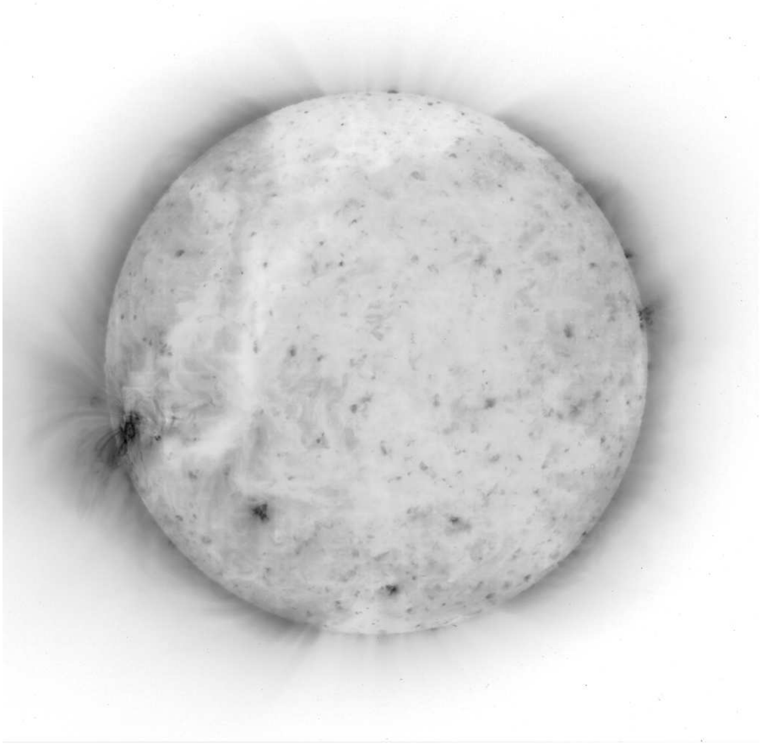

Figure 1.1: An EUV (195 Å) negative image of the solar corona taken on the 25th August 1996, during solar minimum conditions, with one of the instruments on the Solar and Heliospheric Observatory.

When imaged in the EUV (Figure 1.1), the solar corona shows a wide range of different structures, that magnetograms show to be magnetically linked to the underlying and cooler regions of the solar atmosphere, the chromosphere and the photosphere. Between the chromosphere and the corona there is a thin and complex region, the transition region, where the temperature dramatically increases, and which is highly dynamic (for some models of the transition region, see, e.g., *Gabriel*, 1976; *Athay*, 1982).

Most of the corona appears to have a diffuse nature (at modest spatial resolutions) and is referred to as 'quiet sun (QS)'. This quiet corona, which has a mixed-polarity magnetic field, is filled everywhere with small 'bright points (BP)'. Then, in regions with enhanced magnetic field (which in the corresponding visible photosphere appear as sunspots), bright 'active regions (AR)' form, with a multitude of extended loop structures.

The other large-scale structures of the solar outer atmosphere are the coronal holes, which appear as dark features in EUV and soft X-ray images. At the photospheric level, they correspond to a prevalence of unipolar magnetic fields. During solar minimum, the Sun's large-scale magnetic field structure is similar to a dipole, and coronal holes extend over the north and south polar regions, where the magnetic field is mostly unipolar. Occasionally, coronal holes also form in equatorial regions, as shown in Figure 1.1, and described in Chapter 4 of this thesis. Inside polar coronal holes, large-scale ray-like extended features are usually observed, at various wavelengths. Due to their appearance they are named coronal hole plumes.

In the equatorial regions, cusp-like structures form and extend out to large distances: these are called streamers. At even greater distances, the main coronal plasma effect is a stream of fast particles (300-800 km/s) that pervades the solar system: the solar wind. In general, there are many features of the solar outer atmosphere that have been defined and characterized in various ways, in relation to observations with various instruments. It should be borne in mind that these characterisations sometimes merely reflect the limitations in temporal, spectral, or spatial resolution, or areal coverage of the observations performed.

When imaged in lines emitted at temperatures between 100 000 K and a million degrees, in the transition region, the solar atmosphere shows the same pattern as in the chromospheric lines. Magnetograms and measurements of velocity fields show that this pattern is related to the convective motions at the solar surface, which are organised in supergranular cells (about 30 000 Km across, and not to be confused with the smaller photospheric granules), and where magnetic flux is pushed by the plasma motions from the cell-centres toward their boundaries (the so-called network).

The main underlying characteristic of the solar corona is the important role played by the magnetic field in forming and keeping in place all the observed structures. This is because the ratio between gas pressure and magnetic pressure $\beta \ll 1$, i.e. the static structures and the dynamics of the coronal plasma are dominated by the magnetic field. The time evolution of coronal structures is in some way linked to the evolution of the photospheric magnetic field. This surface field is created by dynamo processes acting in the solar interior, which are related to convective motions and are difficult to model.

Although coronal magnetic fields have not been measured directly, there is a large body of evidence suggesting that over large scales streamers represent regions of closed magnetic field, and that the magnetic field lines in the coronal holes open out to interplanetary space. One of these pieces of evidence has been the identification of coronal holes as the sources of the high-speed ($\simeq 800$ km/s) solar wind (*Krieger et al.*, 1973; *Nolte et al.*, 1976), thereby raising interest in the study of coronal holes. This interest has been renewed in recent years since the launch of the Ulysses probe in October 1990. This has produced new in-situ measurements of the solar wind, for the first time out of the ecliptic plane, confirming that the polar holes are the source of the steady high-speed solar wind. Ulysses has also recently shown that the high-speed solar wind fills most of interplanetary space and has fairly constant characteristics, and should therefore be easier to model, compared with the highly-variable low-speed ($\simeq$ 400 km/s) wind that streams out of the equatorial regions (streamer belt). For this reason, considerable interest has developed recently in studying the high-speed solar wind and coronal holes. This is one of the reasons why the work presented in this thesis will mainly focus on coronal holes, although there are many fascinating and unexplained phenomena in the solar corona.

It is also interesting to study plumes, for many reasons. First, they are the only stable observable structures within coronal holes, and although they fill only a small percentage of the solid angle subtended by coronal holes, their contribution to the observed emission along the line of sight is usually significant and important to assess. Secondly, because of their morphology, it is generally assumed that plumes trace the open field lines of the coronal holes and it is therefore important to assess the relationship between plumes and the fast solar wind. Any solar wind model should account for the presence of plumes.

One would expect to derive from the observational data various physical parameters to describe the status of the plasma. These should include for example the elemental abundances, particle velocities and distribution functions, ionic and electron temperatures, densities and magnetic field strengths as a function of space and time. Only in-situ measurements by spacecraft can provide direct information for such parameters. Otherwise, the plasma's physical parameters have to be inferred from remote measurements, i.e. from observations of the solar radiation. Great efforts have been made by various authors to derive values of such parameters from the observations. In particular, EUV spectroscopic observations can provide information on the basic plasma parameters such as temperature, density, element abundances, and flow velocities. Many interesting results have been produced, with the aid of models and various assumptions. These assumptions must always be borne in mind when estimating the values of the deduced physical parameters, and added to the uncertainties in the observations and in the atomic data.

Among the various interesting results, a detailed examination of the Sun's upper atmosphere has revealed that coronal element abundances vary between different solar regions, and are different from their photospheric values, and from those of the solar wind composition. It seems that there is a correlation between the coronal abundances and the first ionization potential (FIP) of the various elements. Low-FIP ($\leq$ 10 eV) elements tend to be more abundant in the corona, relative to those with a high FIP. A large number of papers, often with conflicting conclusions, have been published on this subject (see the reviews by *Meyer*, 1985; *Meyer*, 1993; *Feldman*, 1992a; *Feldman et al.*, 1992b; *Mason*, 1995; *Saba*, 1995; *Meyer*, 1996; *Mason*, 1992; *Phillips*, 1997a). Plumes are particularly interesting in that they represent an extreme case of particular element abundances, in the sense that large FIP biases have been reported from EUV observations close to the limb (*Widing and Feldman*, 1992).

Many theoretical models have been produced to try to explain observations of the solar corona, and although limited by various simplifications, assumptions and the contemporary computational methods, they have been successful in various cases. However, they have failed to satisfactorily answer many general questions, and in particular:

- why is the solar corona a million degrees hotter than the underlying atmosphere ? It is widely accepted that coronal heating takes place when magnetic energy is supplied to the corona, but how and where this is dissipated is still not known;

- why are there variations of chemical abundances in the corona, and what is their relationship with the magnetic field ?

- what is the structure of the transition region, and its relation to the corona ?

- how and where is the solar wind created and accelerated ?

- why do we see coronal holes in the EUV ? Their lower EUV emission is thought to be due to their lower densities and temperatures, even though accurate measurements have been absent. When observed in transition-region lines, the coronal holes are almost indistinguishable from the other regions of the Sun;

- why do coronal holes form, and what is their chemical composition ?

- what is the relationship between coronal holes and plumes ? Are plumes the source of the high speed solar wind ?

- are plumes cooler or hotter than the inter-plume regions ?

Most of these (and many more) questions are still unanswered, for many different reasons. First, the adopted models usually assume various simplifications which might not be justified. In general, the difficulty of the theoretical models in representing the observed structure and dynamics of the solar corona resides in its complexity and in the inter-relations (not yet understood) between the various atmospheric phenomena together with their relation to both the solar interior and the solar wind.

Secondly, the complexity of coronal observations and analysis means that further and more accurate observations are required, including direct measurement of coronal magnetic fields. The EUV region of the spectrum is still relatively unexplored, and many additional uncertainties arise from calculations used in the theory, instrument calibrations and uncertainties in the adopted atomic physics.

Our knowledge of coronal holes is even more limited than that of the corona as a whole. For example, prior to SOHO only one set of EUV spectroscopic data for a coronal hole region existed (*Vernazza and Reeves*, 1978). These data were from the Skylab Harvard College Observatory (HCO) instrument, mounted on the Apollo Telescope Mount (ATM), and until 1996 they were the best source of information about coronal holes in the EUV wavelength range, although the spectral resolution was poor.

SOHO was designed to provide, amongst other things, new observational constraints on the corona and to study in particular the quiet sun around solar minimum. These conditions are the most favourable for studies of polar coronal holes, because they are then at their greatest extent and because of the relative lack of large loop structures. However, projection effects from quiet-sun material along the line of sight can strongly affect both off-limb (see e.g. the comments of *Habbal, Esser, and Arndt*, 1993) and on-disc coronal hole observations.

SOHO has produced a wealth of data and has changed our view of the Sun in so many respects already, and most of the present physical models are being modified or reconsidered in light of the new exciting observations. In particular SOHO observations have already shown the highly dynamic and inhomogeneous structure of the solar corona.

The present research project

The aim of the present research project was to advance our understanding of the solar corona by studying especially coronal holes and their boundaries, using ground-based and SOHO data, and in particular the Coronal Diagnostic Spectrometer (CDS) data. The CDS instrument offered, for the first time, the opportunity of observing emission lines produced by a wide range of temperatures with sufficient spectral resolution to apply spectroscopic diagnostic techniques. The project mainly consisted of: planning CDS coronal hole observations and executing them at the SOHO operations centre, Goddard Space Flight Centre, U.S.; analysing the data, implementing methods with software in IDL (Interactive Data Language); and researching the atomic physics of the CDS spectral lines, in order to determine values for the plasma parameters.

Layout of the thesis

The thesis is organized as follows. Section 1.1 gives an introduction to the theoretical plasma emission, and how temperatures, densities and elemental abundances of the plasma can be obtained from EUV observations. It also introduces the definition of differential emission measure (DEM) and how the multithermal plasma distribution can be studied. Different spectroscopic diagnostic methods are briefly described, leading to a review of coronal observations which is given in Section 1.2. Section 1.2 summarizes observations and theories of the solar corona, with particular reference to coronal holes. It includes a brief description of some of the most recent results from SOHO. This review concentrates on the observational constraints to the models, and how these constraints have been determined, rather than on the theories themselves.

Chapter 2 describes the various diagnostic techniques and the software developed by the author to derive the values of physical parameters from CDS observations. A critical evaluation of the various methods found in the literature is also given. In particular, Section 2.5 presents a re-analysis of Skylab coronal hole spectral data, and compares different methods to deduce differential emission measure and element abundances. Section 2.6 presents a critical discussion of previous work on element abundances.

Chapter 3 describes the CDS instrument and outlines those aspects that limited the possible observations and complicated the data analysis. Then, the CDS data calibration is discussed and new calibrations presented, starting with a description of various preliminary tasks undertaken. The sequence of new CDS observations, planned and executed in order to cross-calibrate the CDS detectors, are fully described. The full CDS line identifications and comparisons of different observations with theoretical calculations are also given in this Chapter.

Chapter 4 details the new CDS observations that were planned and executed in order to study coronal holes, including both on-disc and off-limb observations of polar holes, and on-disc observations of low-latitude holes. The observations were mainly carried out during August 1996, February 1997 and September-October 1997, during solar minimum and the initial rise towards the next maximum. A short description is also given of the methods and software developed for data analysis.

Chapter 5 reports results in terms of morphological descriptions, temperatures, densities and elemental abundances for a selection of the observed coronal structures. First, the general differences in terms of temperatures and densities, between quiet sun and coronal hole regions, as derived from 1996 to 1998 observations, are presented. Then, results from some of the near Sun centre 1996 observations in coronal hole and quiet sun areas are presented and compared.

Chapter 6 is dedicated to on-disc and off-limb coronal hole and plume observations and results. First, the results from the on-disc observations of polar holes are presented and compared to those given in Chapter 5. Secondly, off-limb plume and inter-plume regions are examined in detail, giving examples of 'contamination' from background diffuse non-coronal hole emission. Finally, results from on-disc observations of polar plumes are presented.

Chapter 7 draws together the main results and conclusions of the work, in order to define and characterise coronal holes and plumes in comparison with the quiet sun regions, within the wider range of observed coronal structures.

1.1 An introduction to the theory of emission from coronal plasmas

The *standard model* for coronal emission is adopted in this thesis (see, e.g., *Dere et al.*, 1997, and below for a short description). The best available atomic data have been used, as stored in the CHIANTI databases. The CHIANTI atomic database and analysis software (*Dere et al.*, 1997) is the result of an international collaboration (USA/Italy/UK) to provide a comprehensive dataset for ions of astrophysical interest seen in the wavelength region $\lambda > 50$ Å. Additional information about the CHIANTI atomic database can be found at the CHIANTI homepage:

`http://wwwsolar.nrl.navy.mil/chianti.html`

The Arcetri database (*Landi and Landini*, 1998), produced at the Arcetri Observatory, Italy, has been used for those transitions not included in the CHIANTI database, and as a cross-check. Information on the Arcetri database can be found at:

`http://www.arcetri.astro.it/science/chianti/chianti.html`

The standard model has many assumptions, the main ones being that the plasma is optically thin, hot ($T \geq 10^4$), in a steady state, and in ionization equilibrium. A plasma is in ionization equilibrium when the processes that contribute to the formation of the ions can be decoupled from those affecting the level balance within that ion. These assumptions considerably simplify the analysis of EUV observations. When the plasma is optically thin, it is not necessary to solve the radiative transport equations, in the sense that the observed emission is directly related to the state of the plasma. The results of the theoretical calculations that follow these adopted assumptions will be shown to explain the observed CDS spectra in this thesis with an accuracy often better than the estimated errors on the atomic calculations or the observations. This confirms that for most spectra analysed here, the standard model is applicable.

Another assumption in the standard model is that the particles (electrons and ions) are in thermal equilibrium (i.e. they have a Maxwellian distribution function). This assumption appears justified, since the relaxation time for e-e collisions is $\tau_{ee} \simeq 0.01\ T^{3/2}\ N_e^{-1} = 0.01$ s for $T = 10^6$ K and $N_e = 10^9$ cm^{-3}. The ions also become thermal, after a time longer by the factor $(m_i/m_e)^{1/2} \simeq 43$. After the same time factor, both species are thermalised, and only one temperature need be used: $T = T_e = T_i$. This certainly does not hold for the solar wind, as for example Helios observations have shown (*Marsch*, 1991), and there is an ongoing debate on whether the thermal assumption is in fact valid in the corona, since recent SOHO observations of the upper corona indicate much higher ion temperatures (and different ones for each ion), compared to the electron temperature.

The prevalent atomic processes that take place in the transition region and corona, and the adopted assumptions, are now briefly summarised. Complete descriptions of the emission from coronal plasmas can be found in relevant textbooks and review papers (see e.g. *Mariska*, 1992; *Mason and Monsignori Fossi*, 1994). The main processes are ionization, recombination, excitation and de-excitation. In low density plasmas the collisional excitation and de-excitation processes take place on time scales much shorter than ionization and recombination. Hence collisional excitation dominates ionization and recombination in the populating of the excited states. This allows the low-lying level population mechanisms to be treated separately from the ionization and recombination processes. Radiative excitations are rare due to the weak radiation field. The same applies to stimulated emission. Therefore for permitted transitions the levels are mainly excited by collisions and de-excited by spontaneous radiative decay. In the following, Z_n^{+r} indicates the element of atomic number Z which is r times ionized, in the excited state n, in the sense that n identifies the level, ordered in increasing energy, starting from the ground level $n = 1$ for the ionized state r. $N(Z^{+r})(cm^{-3})$, or more simply N_r will indicate the number density of ion Z^{+r} (i.e. the number of particles per unit volume).

The intensity $I(\lambda_{ij})$ of an optically thin spectral line of wavelength λ_{ij} (frequency ν_{ij}) is:

$$I(\lambda_{ij}) = \frac{1}{4\pi} \int_h P_{ji}\ dh = \frac{h\nu_{ij}}{4\pi} \int_h N_j(Z^{+r})\ A_{ji}\ dh \quad [\mathrm{ergs\ cm^{-2}\ s^{-1}\ sr^{-1}}] \tag{1.1}$$

where i, j are the lower and upper levels, P_{ji} is the bound - bound emissivity (power per unit volume), A_{ji} is the spontaneous radiation transition probability, $N_j(Z^{+r})$ is the number density of the upper level j of the emitting ion, and h is the line-of-sight coordinate. If instead of the intensity, the flux (as, e.g. in whole sun or star observations) is observed, then a similar definition holds, with the integral of the power over the volume of the emitting plasma. Since for allowed transitions we have $N_j(Z^{+r})A_{ji} \sim N_e^2$, the intensity is usually rewritten using the identity:

$$N_j(Z^{+r}) \equiv \frac{N_j(Z^{+r})}{N(Z^{+r})} \frac{N(Z^{+r})}{N(Z)} \frac{N(Z)}{N_{\rm H}} \frac{N_{\rm H}}{N_e} N_e \tag{1.2}$$

where the various terms are defined as follows.

- $N_j(Z^{+r})/N(Z^{+r})$ is the population of level j relative to the total $N(Z^{+r})$ number density of the ion Z^{+r} and is a function of the electron temperature and density. In the coronal model, where every level is collisionally excited from the ground level by the electrons and de-populated via spontaneous emission, $N_j(Z^{+r})$ is proportional to N_e, for allowed transitions. The number density population of level j is calculated by solving the statistical equilibrium equations for a number of low lying levels and including all the important collisional and radiative excitation and de-excitation mechanisms:

$$\begin{aligned} \frac{dN_j}{dt} = & \sum_{i<j} N_i R_{i,j} + \sum_{i>j} N_i A_{i,j} + \sum_{i>j} N_i N_e C^e_{i,j} + \sum_{i<j} N_i N_e C^e_{i,j} \\ & -N_j (\sum_{i<j} A_{j,i} + \sum_{i>j} R_{j,i} + N_e \sum_{i<j} C^e_{j,i} + N_e \sum_{i>j} C^e_{j,i}) \end{aligned} \tag{1.3}$$

  * C^e (cm^{-3} s^{-1}) are the electron collisional excitation rate coefficients.

  * $R_{j,i}$ (s^{-1}) are the stimulated absorption rate coefficients, proportional to the mean intensity of the radiation field.

  * $A_{j,i}$ (s^{-1}) are the spontaneous radiation transition probabilities.

  In practice, because of the short time scales of the relevant processes, it is always assumed that the plasma is in a steady state ($\frac{dN_j}{dt} = 0$). The set of Equations 1.3 is then solved for a number of low lying levels, with the additional requirement that $N(Z) = \sum_j N_j$.

  In the CHIANTI database the processes included are electron excitation and de-excitation, and spontaneous radiative decay. The proton collisional coefficients could also be considered as an additional term, but are not yet included in CHIANTI. The stimulated emission can be neglected in an optically thin plasma.

- $N(Z^{+r})/N(Z)$ is the ionization ratio, and is predominantly a function of temperature.

  Various processes can affect the ionization balance. Since the plasma is optically thin, most of the radiation escapes, the plasma is not in local thermodynamic equilibrium (LTE), and the main processes that regulate the ionization balance are spontaneous radiative recombination, di-electronic recombination and collisional ionization. By considering the detailed balance equations that relate successive ionization stages for these processes, and requiring that the population of ions in a given state is constant with time, it is possible to derive for each state the ratio of two successive ionization stages $N_{Z,r+1}/N_{Z,r}$, which is mainly a function of the temperature, and only slightly depends on the electron density through the rate coefficients. With the additional condition $N(Z) = \sum_r N_{Z,r}$, it is possible to derive the ionization ratio. Many ionization equilibrium calculations have been published in the past, but none include density effects. The most recent ones are those of *Arnaud and Rothenflug* (1985), *Landini and Monsignori Fossi* (1991), *Arnaud and Raymond* (1992), *Mazzotta et al.* (1998).

- $N(Z)/N_{\rm H} \equiv Ab(Z)$ is the element abundance relative to hydrogen.

- $N_{\rm H}/N_e$ is the hydrogen abundance relative to the electron density. This ratio is usually in the range $\sim 0.8-0.9$. H and He, at coronal temperatures, are fully ionized. If we neglect the contribution of the heavier elements to the electron density ($\leq 1\%$), and assume fully ionized H and He, the only parameter that changes this ratio is the relative abundance of He, which is not yet well established. If we assume the *Meyer* (1985) abundances, $\mathrm{N_H/N(He)}$=10 , $N_{\rm H}/N_e = 0.83$; whilst for log ($\mathrm{N_H/N(He)}$)=1.2, $N_{\rm H}/N_e = 0.89$.

The intensity of a spectral line can then be written in the form:

$$I(\lambda_{ij}) = \int_h Ab(Z)C(N_e, T, \lambda_{ij})N_e N_H dh \tag{1.4}$$

with the *contribution function* C given by:

$$C(N_e, T, \lambda_{ij}) = A_{ji}\, \frac{h\nu_{ij}}{4\pi} \frac{N_j(Z^{+r})}{N_e N(Z^{+r})} \frac{N(Z^{+r})}{N(Z)} \qquad (erg\ cm^3\ s^{-1}) \tag{1.5}$$

The *contribution function* contains all of the relevant atomic physics parameters and for most of the transitions has a narrow peak in temperature, and therefore effectively confines the emission to a limited temperature range. In the literature there are various definitions of *contribution functions*, depending on which terms are included. Aside from constant terms, sometimes the elemental abundance and/or $N_{\rm H}/N_e = 0.8$ and/or the term $1/4\pi$ are included in the definition, for example. Throughout this thesis, we will refer to both the contribution functions $C(T, \lambda_{ij}, N_e)$ and to $G(T, \lambda_{ij}, Ab(Z), N_e) \equiv Ab(Z)\ C(T, \lambda_{ij}, N_e)$, i.e. the contribution functions that contain the abundance factor. Also, since the contribution functions will be calculated at fixed density values, and the abundances are independently chosen, in many cases we will simply refer to the functions $C(T)$ and $G(T)$.

At this point, there are many assumptions that can be made, in order to simplify the expression for the intensity. One of the major problems in trying to interpret EUV spectra is that the intensity of the observed spectral line is related to the sum of all the photons emitted into the line of sight. One of the problems is that the current spatial resolution of the EUV instruments is not sufficient to specify the plasma distributions along the line of sight. For example, the same emission can be produced by a low-density plasma occupying a large volume, or by a high-density plasma distributed over only a small fraction of the line of sight.

If a unique relationship exists between $N_{\rm e}$ and T, a differential emission measure $DEM(T)$, a function of only the plasma temperature, can be defined (*Withbroe*, 1978):

$$\int_T DEM(T) dT = \int_h N_e\ N_H dh \tag{1.6}$$

i.e.

$$DEM(T) = \ N_e N_H \frac{dh}{dT} \qquad [cm^{-5} K^{-1}] \tag{1.7}$$

For example, if we assume that the plasma pressure along the line of sight is constant, then from the perfect-gas law $N_e^2 \sim (P^2/T^2)$, and the electron density is only a function of temperature, and the $DEM(T)$ can be defined. The DEM gives an indication of the amount of plasma along the line of sight that is emitting the radiation observed and has a temperature between T and $T + dT$. The DEM is related to the conductive flux and gives information about the structure of the atmosphere.

With this definition, the intensity integral becomes:

$$I(\lambda_{ij}) = Ab(Z) \int_T\ C(T, \lambda_{ij}, N_e)\ DEM(T)\ dT, \tag{1.8}$$

assuming that the abundance of the element $Ab(Z)$ is constant over the line of sight. We therefore have a system of Fredholm integrals of the first species to be inverted, in order to deduce the DEM from a set of observed intensities. More details on the inversion techniques used in the present work can be found in Chapter 2. The integral inversion method has also the advantage that at the same time the DEM distribution and the elemental abundances can be obtained, using a large number of line intensities. This minimizes the effects of errors in observation or theory associated with single lines. Further refinements and considerations of the integral inversion problem, and extensions with the use of an emission measure differential in both temperature and density, can be found in *Craig and Brown* (1976), *Doschek* (1984), *Almleaky et al.* (1989), *Newton et al.* (1995), and *Hubeny and Judge* (1995).

Once the differential emission measure DEM is known, the total emission measure EM can be calculated, integrating the DEM over the whole temperature range:

$$EM \equiv \int_h N_e N_H dh = \int_T DEM(T)\ dT \qquad [\mathrm{cm}^{-5}] \tag{1.9}$$

Sometimes the total emission measure is defined as $EM = \int N_e^2 dh = \int DEM(T) dT$, with the differential emission measure defined as $DEM(T) = N_e^2 (dT/dh)^{-1}$. Following *Pottasch* (1963), various approximations and methods have been introduced in order to approximate the DEM and to deduce elemental abundances, as reviewed in Chapter 2. One method is to define for each observed line an average emission measure $< EM >$, while another is to define for each observed line an averaged $< DEM >$, in order to simplify the inversion of (1.8).

1.1.1 Temperature determination

A first estimate of the plasma electron temperature can be obtained by noting the presence or absence of EUV lines emitted by ions having different ionization equilibrium temperatures. Coronal temperatures can also be estimated from the intensity ratio of pairs of EUV lines, if their contribution function does not depend on density, and assuming an isothermal plasma ($T = T_0$) along the line of sight. If the lines are formed at similar temperatures, it can be assumed that they are emitted by the same spatial structures along the line of sight. The intensity of a line, from a region of constant abundance, can then be written:

$$I_{\lambda_{ij}} = Ab(Z) C(T_0) \int DEM(T)\ dT = Ab(Z) C(T_0) \quad EM \tag{1.10}$$

and therefore the total emission measure can be estimated. From the ratio of two lines of different ions, T_0 can be estimated. The best method is to use lines of the same element and similar ionization stage, in order to make the temperature determination independent of element abundance variations. Examples that apply to CDS will be given in Chapter 2. It should be stressed that the temperatures derived in this way are isothermal temperatures assuming ionization equilibrium. It should also be kept in mind that if the plasma is not homogeneous, the lines emitted by different ions will be generated in different spatial regions, and therefore their ratio has no real meaning except as an average value.

A more direct determination of an isothermal electron temperature, that is not dependent on ionization equilibrium assumptions, can be obtained from the intensity ratio of two allowed transitions to the ground level g of the same ion, from upper levels j and k having significantly different excitation energies E_{gj} and E_{gk}. In fact, if $(E_{gk} - E_{gj})/kT >> 1$, the intensity ratio is temperature-dependent, and assuming that the lines are emitted by the same isothermal volume with the same electron density, an isothermal temperature can be directly deduced from the intensity ratio. This method is difficult to apply because usually the wavelengths of the two transitions are hundreds of Å apart, and therefore the lines need to be observed by different instruments, which must then have a rigorous relative intensity calibration. Temperature-dependent ratios of this type include, for example: O V [629/172], O V [1218/629], and O VI [1032/173]. Examples that apply to CDS observations will be given in Chapter 2.

However, if the plasma distribution along the line of sight is multithermal, as can be expected in most cases, especially for on-disc observations, a more detailed temperature description is obviously needed. This can be obtained from EUV spectroscopic observations via the DEM distribution.

1.1.2 Electron density estimates

An average electron density N_e can be deduced from the total emission measure $< EM >$ and an estimate of the dimension Δh along the line of sight of the emitting plasma (or the volume $V = A_s \Delta h$, with A_s being the observed projected area), assuming that the elemental abundances are known: $< N_e^2 > \sim < EM > / \Delta h$. In most cases, when the $< N_e^2 >$ are compared to the $< N_e >^2$ values that are calculated from direct measurements of the average (along the line of sight) density $< N_e >$ in the transition region, large discrepancies are found. This has been interpreted (*Dere et al.*, 1987) as due to the transition region having a filamentary structure, so that most of the plasma occupies only a small fraction (the filling factor) of the observed volume.

By contrast, no assumption about the size of the emitting volume or the elemental abundances is needed when estimating N_e from density-sensitive line ratios for the same ion.

However, such results still represent an average along the line of sight. The intensity ratio of two lines can become density-sensitive when the two lines have a different dependency on the electron density. For example, for allowed lines the intensity $I_{j,i} \sim N_e^2$ while for forbidden and intersystem lines collisional de-excitation becomes an important de-populating mechanism and the intensity $I_{j,i} \sim N_e$. In general, a ratio of two such lines can therefore be a good density diagnostic, although a temperature dependence can also produce a change in the ratio. There are many cases in which the temperature dependence is so low, and the calculation is performed at the temperature of maximum formation of the ion. Examples that apply to CDS observations will be given in Chapter 2.

Previous estimates of coronal densities have produced a large scatter in the values (see e.g. the SERTS observations, *Brosius et al.*, 1996). Such discrepancies may well be due to uncertainties in the atomic physics or in the instrument calibration, or they could be related to the complexity of structures emitting along the line of sight. In fact, if the plasma is inhomogeneous, different line ratios can easily produce different density values, as *Doschek* (1984) pointed out.

In general, densities deduced from lines emitted at different temperatures should not be expected to be the same, since there is fine structure in the solar corona. This fact has not been fully recognised by many authors. In 'normal' conditions, the density decreases with height. Since the emission is proportional to ${N_\mathrm{e}}^2$, this means that most of the emission will come from the denser (and lower) regions. However, there are many cases where this is not true. For example, if one observes a hot loop in an active region that extends high into the corona, one would expect to measure higher densities from high-temperature lines, because of the contribution from the loop, and lower densities from cooler lines, coming from the other regions in the line-of-sight.

1.1.3 General considerations of the plasma equations

For completeness, this Section introduces some general definitions. Given the high temperature and low density, the coronal plasma follows the perfect gas law:

$$P = \frac{k}{\mu m_H} \rho T = k(N_e T_e + N_i T_i) = 2NkT \tag{1.11}$$

where μ is the mean atomic weight, the average mass per particle in units of proton mass m_H. $\mu = 0.5$ for a plasma of fully ionised hydrogen, while $\mu = 0.62$ for a plasma composed of hydrogen and helium, with a helium abundance $N_{H_e}/N_H = 0.1$. The last equality holds only for a single-fluid plasma, where all the particles have the same temperature

($T = T_e = T_i$ and $N = N_e = N_i$) . The equation of motion for a fluid element (without the viscosity terms) is:

$$\rho \frac{d\vec{v}}{dt} = -\nabla P + \frac{\vec{J}}{c} \wedge \vec{B} + \rho \vec{g} \tag{1.12}$$

where $d/dt = \partial/\partial t + \vec{v} \mathrm{x} \nabla$ is the Lagrangian derivative along the the path, $\vec{J}$ is the current density, $\vec{B}$ the magnetic field, $\vec{g}$ is the gravity acceleration. When the velocity of the fluid element is negligible, compared to the velocity of propagation of sound and magnetic waves, and the velocity of free fall, the equation can be simplified:

$$\frac{dP}{ds} = \rho g \cos\theta \tag{1.13}$$

with $\vec{g} = -g\vec{e}_z$, s the coordinate along the field line that has an angle θ with the vertical $\vec{e}_z$, and $ds \cos\theta = dz$. Using the perfect gas law:

$$P(z) = P_\circ exp\left(-\int_0^z \frac{dz'}{L_P(z')}\right) \tag{1.14}$$

and $L_P = RT(z)/\mu g$ is the pressure scale-height for a single-fluid plasma. In many cases, L_P is much less than the magnetic scale-length, and therefore a constant pressure can be assumed. If the plasma is also isothermal, the density scale-height is the same as the pressure one, and

$$\frac{N(z)}{N(R_\odot)} = \exp\left[-\frac{\mu m_H g_\odot R_\odot}{kT}\left(1 - \frac{R_\odot}{z}\right)\right] \tag{1.15}$$

For a two-fluid plasma, the same equation holds (*Guhathakurta and Fisher*, 1998), with $T = (T_e + T_i)/2$. With these assumptions, is therefore possible to deduce a scale-height temperature T_h from the measured density profiles (*Guhathakurta et al.*, 1992).

The temperature variation along the field lines can be deduced from the heat equation (when the entropy is conserved), considering a flux tube with a cross-section area A:

$$-\nabla \mathrm{x} \vec{F}_c = \tfrac{1}{A}\tfrac{d}{ds}\left(\chi_\circ T^{5/2} A \tfrac{dT}{ds}\right) = E_R(T) - E_H(T) \tag{1.16}$$

that is simply a balance between thermal conduction $\nabla \mathrm{x} \vec{F}_c$, radiative losses $E_R(T)$ and heating processes $E_H(T)$. $\chi_\circ$ is the coefficient of conduction (*Spitzer*, 1965). The thermal conduction is very efficient along the field lines; the heating function is usually parameterised; the radiative loss function for the coronal plasma is:

$$E_R = N^2 \Lambda(T) = \frac{P^2}{4k^2T^2}\Lambda(T) \quad erg\ cm^{-3}\ s \tag{1.17}$$

where $\Lambda(T)$ is the sum of all the emissivities of the coronal lines (total power per unit emission measure). Once the DEM distribution and the $\Lambda(T)$ are calculated, the total luminosity $L = \int_T DEM(T)\ \Lambda(T)\ dT$ emitted by the plasma can be derived. Once the DEM is known, it is straightforward to deduce the temperature gradient along the line of sight, assuming that the temperature is a single-valued function, and to deduce the temperature, once a value for the pressure is fixed.

1.2 Previous observations of the solar corona

1.2.1 Ground and space observations of the solar corona

The main observations of the solar corona consist of X-ray and EUV observations, radio brightness measurements and brightness and polarization of the white-light emission. The photospheric magnetic fields are provided as magnetograms, and the distribution of sunspots indicates the level of magnetic activity. Magnetograms, H_α, Ca H and K images, have been and continue to be provided by many ground based observatories.

Many observatories around the world take daily observations of the solar corona. For example, the Mauna Loa Solar Observatory K-coronameter has provided white-light data since 1965. Infrared observations in the absorption line of He I (10830 Å) have been taken continuously since 1977 with the Vacuum Solar Telescope at the Kitt Peak National Observatory, and are also provided by other observatories (e.g. Pic du Midi).

Observations in the visible part of the spectrum are particularly interesting in the green and red coronal lines Fe XIV 5303 Å and Fe X 6374 Å , since their intensity is lower in coronal holes (especially Fe XIV), whereas intensities of other lines, (e.g. H_α and Ca II K) and the continuum are not reduced. Coronal-line intensity measurements at 1.15 $R_\odot$ are carried out daily at the National Solar Observatory at Sacramento Peak (NSO/SP), New Mexico. Fe XIII 10798 and 10747 Å , Si X 14301 Å are also observed (*Penn and Kuhn*, 1994).

Solar radio observations are provided for example by the Nobeyama and Nancay radioheliosopes.

Space observations pre-SOHO

Many rocket flights and satellites have provided EUV observations of the solar corona. Some of them are listed in Table 1.1. After some early rocket flights, the first series of small satellites were the Orbiting Solar Observatories (OSO). The main sources of EUV

Table 1.1: Some space-borne instruments that observed the solar corona in EUV.

Instrument	Dates	λ [Å]	$\delta\lambda$[Å]	δS (arc sec)	$\delta t(s)$	FOV	references
OSO IV	1968	300-1400	3.2	60	900 full scan	1x1	*Reeves and Parkinson* (1970)
Rocket	1969	50-300	0.25	-	-	integrated Sun	*Malinovsky and Heroux* (1973)
LASP (rocket)	1969	60-385					*Behring et al.* (1972)
OSO V	1969	25-400	$\sim$ 0.4		900 full scan	integrated Sun	*Kastner et al.* (1974)
OSO V	1969	280-370 465-630 760-1030	integrated	none	2	integrated Sun	*Kastner et al.* (1974)
OSO VI	1969	280-1390	3.2	35	900 full scan	1x1	*Noyes* (1971); *Reeves and Parkinson* (1970)
OSO VII	1972	150-400	0.85	20	120	5x5	*Kastner et al.* (1974, 1976)
Rocket	1973	140-873	0.17	-	-	disc centre	*Firth et al.* (1974)
LASP (rocket)	1973	160-770	0.06	-	-	-	*Behring et al.* (1976)
Skylab S-O55 (HCO)	1973-4	280-1350	1.6	5	$\sim$ 330	5x5	*Reeves and Parkinson* (1970); *Vernazza and Reeves* (1978)
Skylab SO82-A (NRL)	1973-4	171-630	0.1	$\geq$ 2 slit-less	none	full Sun images	*Feldman* (1987); *Dere* (1978a)
Skylab SO82-B (NRL)	1973-4	970-3940	0.04-0.08	slit 2x60			*Bartoe et al.* (1977)
CHASE	1985	160-1344	0.25-0.4	15	few sec.	3x1 max	*Breeveld et al.* (1988)
NIXT	1988	63.5	wide band	2-3	none	full Sun images	*Golub et al.* (1990)
MSSTA (rocket)	1991	40-2800	few bands	0.7	none	full Sun images	*Walker et al.*, (1993)
SERTS	1989-	235-450 (170-225 IIo)	0.06	6	none	5x8	*Brosius et al.* (1998a)

data for twenty years have been the instruments flown on Skylab (1973-1974). Three Skylab workshops summarised the main findings: on coronal holes and the solar wind (*Zirker*, 1977); solar flares (*Sturrock*, 1980); and solar active regions (*Orrall*, 1981). Coronal brightness and polarization using a broad bandpass have been measured by the white light coronagraph (WLC) on Skylab. These data have been used by various authors to deduce coronal densities (see below).

One of the main instruments was the Harvard College Observatory EUV spectrometer S-O55 (HCO), on the Apollo telescope mount (ATM). The Skylab HCO spectrometer had good spatial resolution in the 280 Å - 1350 Å range, but low spectral resolution ($\simeq$ 1.6 Å). This limited the information that could be extracted from these data and might explain why many studies based on these data have produced conflicting results. In the standard grating position, the instrument scanned six wavelengths typical of chromospheric to coronal temperatures: Lyα (1216 Å, $T \simeq$ 2x10^4); C II (1336 Å, $T \simeq$ 3.5x10^4); C III (977 Å, $T \simeq$ 7x10^4); O IV (554 Å, $T \simeq$ 1.5x10^5); O VI (1032 Å, $T \simeq$ 3x10^5) and Mg X (625 Å, $T \simeq$ 1.1x10^6). With other grating positions, spectroheliograms of the lines Ne VII (465 Å, $T \simeq$ 5x10^5) and Si XII (521 Å, $T \simeq$ 1.8x10^6) were also recorded. The good spatial resolution of the HCO spectrometer enabled *Vernazza and Reeves* (1978) to produce a list of line intensities for different solar regions. As already mentioned, these data include the *only* coronal hole spectra in that wavelength range obtained before SOHO.

Skylab observed many mid-latitude coronal holes, classified by *Nolte et al.* (1976) as CH 1,2,.... The principal one (CH 1) was already formed when Skylab started its observations, and is known as the 'Italy boot-shaped' coronal hole, due to its famous appearance. It extended N-S from the north pole to southern latitudes, and passed the central meridian on November 21-22 1973. No other such elongated coronal holes were observed by Skylab. The photospheric magnetic field was predominantly of positive polarity within the coronal hole, the same as the north pole and the polarity of the *following* parts of northern-hemisphere active regions. It was surrounded by predominantly negative polarity. A magnetogram taken one rotation before the first Skylab CH 1 observation showed an active region (at $\sim 15^o S$) with positive *leading* polarity. Therefore, the unipolar region probably formed from the decay of the active region flux (*Timothy et al.*, 1975; *Wang and Sheeley*, 1993).

After Skylab, the Coronal Helium Abundance Spacelab Experiment (CHASE) on the Spacelab 2 Mission was a specific mission to determine the helium abundance from the ratio of He II 304 Å to Lyman-α 1218 Å, on the disc and off the limb.

In addition, rocket borne EUV spectrometers were developed at the University of Colorado. The first high resolution images of the Sun using the multi-layer technique were obtained in 1987 by *Walker et al.* (1988) at around 171-175 Å(Fe IX, Fe X) and at 256 Å (He II, Fe XXIV). In 1989, *Golub et al.* (1990) obtained an image with a normal incidence X-ray telescope (NIXT), with a filter centred at around 63.5 Å (Mg X, Fe XVI). The Multi Spectral Solar Telescope Array (MSSTA) was first flown in 1991 (*Walker et al.*, 1993) and produced sub-arc-second resolution (0.7") images in Lyman-α and Fe XII (193 Å) and 1.5" images in Fe XIV (211 Å).

The Solar EUV Rocket Telescope and Spectrometer (SERTS), developed at the Goddard Space Flight Center, has been flown several times since 1989, and has produced both non overlapping spectroheliograms and stigmatic spectra (slit $4.9'$ by 7") of the same solar region. SERTS has observed many quiet sun and active regions, but has not observed coronal holes. Given its high spectral resolution, and an overlap with the wavelengths observed by CDS, the SERTS observations are particularly important, especially for instrument calibration purposes. A re-examination of the SERTS 1989 observation (SERTS-89) is presented in Chapter 3.

Finally, it should be noted that many other satellites and instruments have observed the solar corona, and in particular coronal holes at both X-rays and UV wavelengths. For example, Yohkoh is a successful satellite that has observed the solar corona in X-rays, with four instruments. It was mainly designed to study energetic phenomena such as flares, and not coronal holes. Various High Resolution Telescope and Spectrometer (HRTS) rockets, developed at the Naval Research Laboratory (NRL), have observed in the UV the solar transition region. The sixth one, flown on November 20th, 1988 observed a coronal hole on the disc.

EUV line lists and identifications.

Despite the large number of observations of the solar corona, very few EUV spectral observations have been sufficiently complete and accurate to allow extensive line lists and identifications to be made. The most important studies for direct comparison with CDS are listed here.

Malinovsky and Heroux (1973) were among the first to apply the *Pottasch* (1963) emission measure method to confirm or reject previous identifications in the 50-300 Å range, using an integrated Sun spectrum with 0.25 Å resolution taken with a grazing-incidence spectrometer flown on a rocket in 1969.

Firth et al. (1974) give a line list in the 140-870 Å range, based on U.K. rocket observations, with 0.17 Å resolution.

Behring et al. (1976) present a high-resolution (0.06 Å) spectrum in the 160-770 Å range of the entire Sun, taken with a rocket flight. The lines were identified based on their position, and the intensities were only approximate.

Dere (1978a) presented a list of line identifications based on all the flare observations of the NRL SO82-A instrument aboard Skylab, in the 171-630 Å range, with 0.1 Å resolution. This list is therefore biased toward high-temperature lines. *Dere* (1982) presents an extensive list of lines from spectra of active regions observed with the same NRL SO82-A instrument.

The SERTS-89 observation has been described by *Thomas and Neupert* (1994), including a useful line list in the 170-450 Å range, based on high resolution well calibrated spectra. More details can be found in Chapter 3, where this observation is re-analysed.

Space observations: SOHO

Details of the SOHO project and its instruments can be found in a special issue (Vol. 162) of the Solar Physics journal (1995). More information on the publicly-available data and software databases can be found on the World Wide Web:

`http://sohowww.nascom.nasa.gov/`

The 12 instruments on SOHO are:

- SUMER (Solar Ultraviolet Measurements of Emitted Radiation) is a normal incidence spectrometer in the 500 to 1610 Å band, with high spatial resolution (1.2-1.5$''$) and high spectral resolution ($\frac{\lambda}{d\lambda}$ = 19 000 to 40 000). Doppler velocities and line broadenings can be measured down to 1 km/s separately for each spatial resolution element.

- The CDS instrument, described in *Harrison et al.* (1995), consists of two instruments: a Normal Incidence Spectrometer (NIS) and a Grazing Incidence Spectrometer (GIS), which overall cover the 151-785 Å spectral region [with two channels in normal incidence (NIS 1, NIS 2) and four channels (GIS 1, GIS 2, GIS 3, GIS 4) in grazing incidence] at moderate resolution (0.35-0.5 Å). CDS can observe coronal diagnostic lines on the disc, unlike SUMER. More details on CDS, including data reduction methods, can be found in Chapter 3.

- UVCS (Ultraviolet Coronagraph Spectrometer) can perform spectroscopic observations between 2 and 10 $R_\odot$ from sun centre and produces line profiles of Lyα, O VI, Fe XII and many other ions. It allows a determination of proton velocity distribution, proton outflow velocity, electron temperature, and ion outflow velocities and densities.

- EIT (Extreme ultraviolet Imaging Telescope) is a normal-incidence, multi-layer telescope which covers the full solar disc (1024 x 1024 pixels with a field of view of 45'x45'). Subfield images can be created in four band-passes: Fe IX 171 Å, Fe XII 195 Å, Fe XV 284 Å and He II 304 Å. The pixel resolution is $2.6''$.

- LASCO (Large Angle and Spectrometric Coronagraph Experiment) is a set of three coronagraph telescopes that image the solar corona in white light from 1.1 $R_\odot$ to 30 $R_\odot$ (C1: 1.1 to 3 $R_\odot$; C2: 1.5 to 6 $R_\odot$; C3: 3.5 to 30 $R_\odot$).

- VIRGO (Variability of solar IRradiance and Gravity Oscillations) has two types of active cavity radiometers that are measuring the spectral irradiance and radiance variations on time scales down to minutes. These monitor the solar irradiance (formerly known as the *solar constant*).

- GOLF (Global Oscillations at Low Frequencies) measures doppler shifts of sodium absorption lines, deducing mean disc line-of-sight velocities, to study p and g modes of the solar non-radial oscillations.

- MDI (Michelson Doppler Imager) images the Sun on a 1024 x1024 CCD camera through a series of increasingly narrow filters (Michelson interferometers) and polarizers, giving a full-width-half-maximum (FWHM) bandwidth of 100 mÅ centred on Ni I 6768 Å. Velocity and magnetic field line-of-sight components and continuum intensity can be determined once per minute, with a resolution of $4''$ over the whole disc. A higher resolution is also achievable with a smaller field of view.

- SWAN (Solar Wind ANisotropies) measures Lyman alpha UV light scattered by interplanetary H I, in order to determine the large scale solar wind distribution.

- Particle instruments study the solar wind and the solar energetic particles (SEP): COSTEP (Comprehensive Supra-thermal and Energetic Particle Analyzer); CELIAS (Charge, Element, and Isotope Analysis System); ERNE (Energetic and Relativistic Nuclei and Electrons experiment).

1.2.2 General coronal hole characteristics

Following the first EUV observations, coronal holes were defined (*Reeves and Parkinson*, 1970) as those areas with much lower (by factors up to 10) intensities of coronal lines (e.g., Mg X 625 Å). It should be noted that such a simple definition of coronal hole areas can be misleading. In fact, the so-called *filament channels* also appear as thin long regions of low intensity in coronal lines. Filament channels are usually (but not always) associated with stable dark H_α chromospheric features. Characteristic features that differentiate *filament channels* from coronal holes, are: (1) X-ray arches cross over a channel but diverge in a coronal hole; and (2) *filament channels* lie along neutral lines.

In the lines emitted from the transition region, it is difficult to recognize coronal holes. Studies based on Skylab and HRTS data (*Huber et al.*, 1974; *Dere et al.*, 1989) have shown that transition region lines have almost the same intensity distribution inside and outside coronal holes, with the only difference that the brightest supergranular cell boundaries (network) are depressed in coronal holes (by about 50 %). Transition region lines produce limb-brightened rings that in coronal hole areas are both elevated (10-15") and wider (5-8" in width), compared to the quiet sun regions (*Withbroe and Noyes*, 1977). This observation has been interpreted in the sense of a larger range of heights over which the lines are formed, and therefore indicates a lower temperature gradient in coronal holes. As a result, the heat flux conducted from the corona to the transition zone is much smaller (by an order of magnitude) in the holes than in the quiet sun.

In chromospheric lines, coronal holes are once again clearly visible. For example, in the EUV He I and He II emission lines, the network within the holes is about 50% of the intensity of the quiet sun. Because chromospheric lines do not have the problem of foreground emission that coronal lines have, they can be used to trace the hole boundaries. In the visible part of the spectrum, the network areas show stronger He I absorption both inside and outside coronal holes, while the cell centres have lower He I absorption. On the average, coronal hole areas have lower He I (10830 Å) absorption than the other areas, and therefore the equivalent width of this line has become a commonly used diagnostic for defining coronal holes. It is interesting to note that in transition region lines, coronal holes sometimes show large jets of plasma (*macrospicules*), that are not visible in the quiet sun. Macrospicules differ from the H_α spicules in that their average width, height and lifetime are all much greater, and also that they tend to be radial, whilst spicules have no preferred inclination.

Bocchialini and Vial (1996) analysed the profiles observed by the OSO-8 spectrometer inside and outside of the equatorial coronal hole which was at the centre of the solar disc between 27 and 29 November, 1975. After separating coronal hole and quiet sun profiles and taking an average, they found stronger Hydrogen L_α (40 %) and Mg II k profiles (25 %)in the coronal hole, compared to the quiet sun. Network L_α intensities, on the other hand, are very similar. This result is rather surprising, and at variance with other Skylab observations (e.g. *Vernazza and Reeves*, 1978).

In terms of physical parameters, previous coronal hole observations (see the reviews of *Habbal, Esser, and Arndt*, 1993; *Withbroe*, 1988; *Hara et al.*, 1994), based primarily on Skylab data, have shown coronal holes to be regions of lower coronal density and temperature. However, the various results are not in very good agreement with each other, and are not as precise as the theoretical solar wind models require (*Habbal, Esser, and Arndt*, 1993). More details on how coronal hole densities and temperatures have been estimated are given in the following Sections.

Coronal hole area, distribution and rotation

He I 10830 Å observations during the period 1978-1991 have been used by various authors (e.g. *Insley et al.*, 1995) to study the distribution of coronal holes. This large dataset has shown that in the declining phase of the solar cycle and at solar minimum, the polar coronal holes dominate, and have equator-ward extensions, while there are but few low-latitude coronal holes. Around solar maximum, on the other hand, mid-latitude coronal holes dominate, and have a large spread in latitude. The time variation of the distribution of mid-latitude holes follows the same equator-ward trend as the sunspots. In addition, the mid-latitude coronal holes exhibit significant differential rotation, although not as pronounced as that observed for sunspots. However, the equator-ward extensions of polar coronal holes show no differential rotation.

Timothy et al. (1975) using Skylab data, deduced that although the structures that delineate the hole boundary change significantly, coronal holes rotate almost rigidly, with only a slight distortion due to the solar differential rotation. The rotation rate is almost equal to that of the sunspot equatorial rotation. After the Skylab era, other coronal holes were observed, some of which showed significant differential rotation (*Wang and Sheeley*, 1993), while others (*Tsuneta and Lemen*, 1993, from Yohkoh observations) apparently did not.

The boundaries of coronal holes change in short timescales and those are related to appearances or disappearances of bright points, according to *Kahler and Moses* (1990). These authors explain the boundary changes using a magnetic reconnection scenario. In particular, *Wang and Sheeley* (1993) explain the formation of the Skylab CH 1 in terms of an interaction between the axisymmetric polar field and the non-axisymmetric photospheric flux, in the form of a decaying active region located at low southerly latitude. In general, it is therefore concluded that equatorial coronal holes rigidly rotate during the declining phase of a solar cycle, when an active region erupts at low latitudes and interacts with the polar fields. Conversely, during the rising and maximum phases of the cycle, non-axisymmetric photospheric flux tends to be present at higher latitudes, and coronal holes tend to shear and rotate differentially at the local photospheric rate.

1.2.3 Temperatures

Coronal hole temperatures have previously been estimated using various methods assuming an isothermal plasma. *Habbal, Esser, and Arndt* (1993) review the range of temperatures that have been deduced from remote (e.g., spectroscopic) measurements of coronal holes, within a distance of 1.6 $R_\odot$, and they also review the accuracy to which these temperatures have been determined. *Withbroe* (1988) also reviews coronal hole temperature measurements, and those are critically discussed below. Apart from the in-situ measurements, all others can be usefully separated into those observations made on the disc, and those made above the limb. Observations above the limb have the advantage that physical parameters like temperature and density can be measured as a function of the radial distance. However, care must be taken to allow for foreground and background quiet Sun emission along the line of sight (see, e.g., *Esser et al.*, 1995), which (on the other hand) can be a small effect for on-disc observations.

Temperatures from in-situ charge state measurements

Empirical constraints on the temperatures at the "freezing-in radius" have been derived from charge state measurements at 1 AU. The freezing-in radius is the distance from the Sun centre where the expansion time of the solar wind equals the equilibrium timescale between the ions. Various assumptions must be made in order to deduce such temperatures, e.g.: assumptions about the expansion model, the charge state distribution, the elemental abundances, the distribution function of the electrons and the relative flow speed of the different charge states. *Galvin et al.* (1984) found a value of 1.3 ± 0.2 MK at 1.5 $R_\odot$ from CNO ions, while *Ipavich et al.* (1986) derived values of 1.3 ± 0.3 MK at 1.5 $R_\odot$ from CNO ions and 1.4 ± 0.2 MK at 3 $R_\odot$ from Fe ions. For recent results from Ulysses SWICS data and models, see *Ko et al.* (1997).

Temperatures above the limb from white light observations

Analyses of white-light coronagraph observations have been used to derive the radial density profile from the measured intensity of the polarized brightness of the K corona, following *van de Hulst* (1950). Assumptions about the F corona contribution and the density distribution along the line of sight produce additional uncertainties in the densities. Then the temperature can be derived, assuming an isothermal atmosphere in hydrostatic equilibrium. Clearly, the deduced temperatures can only be rough estimates.

Temperatures from Lyα profiles

Several coronagraph experiments (e.g. Spartan, SOHO/UVCS) have provided temperatures above polar coronal holes from Lyα profiles (see, e.g., *Withbroe et al.*, 1986; *Kohl et al.*, 1980). The spectral line profiles, at the distances observed by these instruments, have two components. The resonantly scattered, relatively narrow component provides empirical constraints on the electron and proton temperatures. The weaker, electron scattered component is wider and related to the electron density and temperature. This method provides effective temperatures rather than kinetic temperatures, and therefore the reported values can be used as upper limits to the temperature of the coronal plasma.

Limb observations from EUV intensities

Many early studies, instead of directly measuring temperatures, deduced them from observations of radial intensity profiles off-limb, and an appropriate model. For example, *Krieger et al.* (1973) inferred a temperature of 1.3 x10^6 K at a distance 1-1.14 $R_\odot$ in a south polar coronal hole using X-ray images of a rocket flight on 1970 November 24. They deduced X-ray intensities from photographic densities, and from these they derived the density scale height and finally the temperature, assuming an isothermal spherically symmetric model. *Mariska* (1978) derived the off-limb temperature of a polar coronal hole on 14th August 1973 (near solar minimum), using the spectroheliograms of the HCO instrument on Skylab. The radial intensity profile of five EUV lines of different elements were fitted with an empirical model that assumes an isothermal corona in hydrostatic equilibrium. The derived parameters are the density (1.7 x10^8 cm^{-3}) and conductive flux (6 x10^4 ergs cm^{-2} s^{-1}) at the base of the corona which was assumed to be 1.03 $R_\odot$, together with a coronal temperature of 1.1 x10^6 at 1.08 $R_\odot$. The model then yields a temperature of 7.6 x10^5 K at 1.03 $R_\odot$. A *DEM* analysis was also performed.

Other studies have derived isothermal temperatures from line ratios, but in most cases lines emitted by different elements were used, and this limits the accuracy of the temperatures inferred. For example, *Habbal, Esser, and Arndt* (1993) present some estimates of off-limb temperatures, from analysis of 1973 December 13 Skylab S-O55 spectroheliograms, using intensity ratios of the lines Mg X (625 Å), Ne VII (465 Å), and O VI (1032 Å). These were limb observations of a south polar coronal hole and its neighboring quiet regions. The authors assert that there is very little contamination from quiet region emission along the line of sight. They obtain a temperature range of 7.8-9.3 x 10^5 K, between 1.02 and 1.07 $R_\odot$ for the coronal hole, and 9.4 x 10^5 - 1.2 x 10^6 K for the quiet regions bordering it, where this quoted range in temperatures is due to inhomogeneities within the coronal hole itself. The authors carefully take account for possible abundance variations. They varied the theoretical abundances of the three observed elements (Mg, Ne, O), to obtain the best agreement between abundances and temperature. This was probably the most accurate pre-SOHO work, in terms of temperature measurements based on EUV lines, and it gives an idea of how the paucity of data affected the attempted measurements.

Guhathakurta et al. (1992) derived temperatures from the intensity ratio of two Fe XIV lines: the 173 Å line recorded by a rocket; and the green 5303 Å line from ground-based observations. They found an average coronal temperature of 1.34 x 10^6 K for a south polar coronal hole and 1.27 x 10^6 K for a north polar coronal hole, at 1.15 $R_\odot$, during the 1988 March 17-18 solar eclipse. They also deduced temperatures from density scale heights deduced from contemporaneous white light coronagraph observations, but these values (0.95 and 1.1 x 10^6 K) are not in agreement with the previous ones.

Esser et al. (1995) analysed daily intensity measurements at 1.15 $R_\odot$ of the green Fe XIV 5303 Å and red Fe X 6374 Å lines. Their main finding is that the coronal hole temperatures derived using the line ratio technique vary by more than 0.8 x 10^6 K over the time interval of the observations which covered about four solar rotations. They also discuss how the regions surrounding the coronal holes might influence the temperature gradient in the coronal holes.

Disc observations and emission measure analysis

Direct EUV observations on the disc have been rare, and so on-disc temperatures of coronal holes were also scarce. For example, using OSO-4 data, *Munro and Withbroe* (1972) found a coronal hole temperature of 1.05 x10^6 K, assuming constant electron pressure and temperature gradient.

The most complete description of the distribution of plasma at different temperatures is given by a DEM analysis. Only a few DEM analyses have been performed on coronal hole EUV spectra (*Munro and Withbroe*, 1972; *Raymond and Doyle*, 1981b; *Dere and Mason*, 1993; *Doschek*, 1997a; *Mason et al.*, 1997).

Raymond and Doyle (1981b) derived a DEM from the 'Italy' coronal hole observed by Skylab, using the averaged cell-centre and network intensities of *Vernazza and Reeves* (1978). See Chapter 2 for a re-analysis of these data.

Doschek (1997) have deduced emission measures using high-resolution NRL S082-B Skylab spectra of different regions (including coronal holes). In this case the information was limited by the fact that only transition region lines in a restricted temperature range ($3\text{x}10^4 - 2.5\text{x}10^5$ K) were observed at the limb.

Temperatures from filter ratio techniques

Finally, temperatures have also been estimated by many authors from soft X-ray or EUV broad-band filter images, this method uses the intensity ratio of two filters in which emission comes mainly from plasma at distinct temperatures for the respective two filters. For example, *Hara et al.* (1994) estimate the temperatures of a large coronal hole that extended to both northern and southern hemispheres, with the filter ratio technique of *Tsuneta et al.* (1991), applied to the Soft X-ray Telescope (SXT) aboard Yohkoh. The estimated coronal hole temperatures are 1.8-2.4 x 10^6 K, almost the same values as those derived for quiet regions. The Yohkoh X-ray filter ratio technique therefore yields coronal hole temperatures around 2 MK (as confirmed by *Hara*, 1997), a result that contradicts other estimates (e.g. by almost a factor of two higher than from EUV spectra). This fact has puzzled many researchers. Yohkoh observes coronal X ray emission from a broad range of plasma temperatures above $1\text{x}10^6$ K, and with a sensitivity biased toward hotter emission in the 3–$6\text{x}10^6$ K range. A possible explanation for the apparent discrepancy is then the presence of hot material in the line of sight.

In general, these *filter ratio techniques should be avoided*, if possible, for a variety of reasons. First, the lines that contribute to the emission observed through one filter, will not normally be formed at the same temperatures, and hence might not be emitted by the same spatial regions: the filter does not then sample isothermal plasma. Secondly, the lines in a broad-band emission, might derive from different elements (as is the case for the Yohkoh filters), and therefore assumptions about element abundances have to be made, thus increasing the uncertainty in what is already only an average temperature.

1.2.4 Densities

The density measurements that differentiate between coronal holes and plumes will be described in Section 1.2.6. Most studies (e.g., *Munro and Jackson*, 1977; *Guhathakurta et al.*, 1993; *Guhathakurta and Holzer*, 1994) have estimated the electron density following the *van de Hulst* (1950) method.

Many other authors have derived densities from the intensity gradients in off-limb observations. For example, *Mariska* (1978), as already explained, derived a density of $1.7\text{x}10^8$ cm^{-3} for the 14th August 1973 polar coronal hole, a value remarkably close to the values subsequently derived by SOHO.

Other recent studies have determined the temperature and density structure of the solar corona from a combination of K-coronal and polarization brightness (from eclipse or coronagraph observations), the green and red coronal forbidden lines, and EUV images from a sounding rocket (e.g. *Guhathakurta et al.*, 1996).

Crude estimates of densities have also been obtained from the emission measure method. For example, *Hara et al.* (1994) estimated the total emission measure of a coronal hole from Yohkoh observations, and found values in the range $10^{25.5}$ - $10^{26.2}$ cm^{-5}, about ten times smaller than those of quiet regions. Therefore, if their deduced temperatures and EM values are correct, it follows that the observed lower soft X-ray intensity of the coronal hole regions is due to a density that is lower by a factor of 3 compared with the quiet regions.

However, as mentioned above, the most accurate method is to use density-sensitive ratios of lines emitted from the same ion. In the past, very few such EUV observations have been performed, and none successfully used coronal lines to deduce coronal hole densities, before SOHO was launched. *Dwivedi and Mohan* (1995a) estimated the electron density in a coronal hole using the Mg VIII density-sensitive theoretical line ratio [436.62 / 430.47], and Skylab HCO data, to find an electron density $N_e = 3.4\text{x}10^7$ cm^{-3} for the coronal hole, compared to $N_e = 5.8\text{x}10^7$ cm^{-3} for the quiet sun, using the *Vernazza and Mason* (1978) data. However, the HCO data were affected by blending, as the same authors pointed out.

It is only with SOHO that, for the first time, line-ratio techniques have been fully applied to obtain coronal hole densities. *Doschek et al.* (1997b) applied a ratio technique to coronal lines (Si VIII and S X) in SUMER off-limb observations. They found the coronal hole densities to be systematically lower than those in the quiet sun, by a factor of about 2. Similar results, based on a much more complete data set, were found during this thesis work, as described in Chapter 5. *Laming et al.* (1997a) also present off-limb SUMER observations, and deduce densities from various coronal line ratios. More recently, *Warren and Hassler* (1999) accurately measured off-limb densities at a height between $10''$ and $20''$ from the limb, using many lines from SUMER, and found densities $N_{\rm e} \simeq 10^{8.35}$, with a small scatter.

Regarding measurements of electron densities at lower heights, i.e. from lines emitted at lower temperatures in the transition region it should be noted that before SOHO even quiet-sun results were very rare, and had large uncertainties. This was due to the low spectral resolution and low sensitivity of the previous instruments. *Munro and Withbroe* (1972) were among the first to attempt a measurement of transition region densities in coronal holes using OSO IV spectra and the C III 1176/977 Å density-sensitive ratio. As the authors reported, the data did not allow a reliable measurement of the density. However, some coronal hole areas were found to have densities a factor of two to three lower than the quiet sun regions. *Dupree et al.* (1976) analysed Skylab HCO data and found significant variations in the C III 1176/977 Å ratio, for different solar regions, with an average value for the quiet sun of 0.29, yielding a density $N_e = 4.6\text{x}10^9$ cm^{-3}. A trend for higher densities in the cell centres was also found, although in the quiet sun regions the uncertainty was large. *Vernazza and Reeves* (1978) derived densities from the same C III 1176/977 Å lines observed by the Skylab HCO instrument, but found $N_e \simeq 1\text{x}10^{10}$ cm^{-3} from the averaged spectra, with no differences between coronal holes and quiet sun. Moreover, differences were found between the cell centres and network regions, but this time with the network having larger (by about a factor of two) densities than the cell centres, in contradiction to the previous analyses done by *Dupree et al.* (1976). However, the density sensitivity of this C III ratio is small and furthermore C III could be affected by some opacity effects.

Various authors used the Skylab NRL S082-B to deduce densities. However, only observations close to the limb could be used for density diagnostics. *Doschek et al.* (1978) presented densities for coronal holes and the quiet sun close to the limb, using C III, O III, and Si IV lines, finding an averaged value $N_e \simeq 1.9\text{x}10^{10}$ cm^{-3} for the quiet sun regions, with no differences in the polar coronal hole, except in one case where a lower density (by a factor of 2) was found. *Cook and Nicolas* (1979) also derived densities for coronal holes and the quiet sun from Skylab NRL S082-B observations close to the limb, using C III, Si III and Si IV lines, finding densities in the range $N_e = 3\text{x}10^9 - 2\text{x}10^{11}$ cm^{-3}, with most of the values at the limb $N_e \simeq 1\text{x}10^{10}$ cm^{-3}, and with no differences between quiet sun and polar coronal holes. Recently, *Doschek* has re-analysed some of the NRL S082-B observations, comparing the results that are obtained using different instrument calibration, and using more recent atomic data. The results from O V, Si III, C III showed discrepancies, that moreover could not be easily explained by a wrong calibration. Densities had a large scatter of values around $N_e \simeq 1\text{x}10^{10}$ cm^{-3}, depending on the ratio and/or the instrument calibration adopted, with the coronal hole having consistently lower values.

Cook et al. (1995) present O IV and Si IV density diagnostics in the UV range applied to solar and stellar spectra. From HRTS and Skylab S082-B observations of the quiet sun and active regions, but not coronal holes. Large discrepancies were also found there, with one O IV ratio producing a value of $N_e = 5\text{x}10^9$ cm^{-3} for the quiet sun region. *Keenan et al.* (1995) present new calculations for O V diagnostics and apply the 1371.29 Å / 1218.35 Å ratio to HRTS and Skylab S082-B observations at the limb, of coronal hole, quiet sun, and active regions. a density $N_e = 3\text{x}10^{10}$ cm^{-3} for a coronal hole region observed by the Skylab instrument was found, with no differences from the quiet sun values. In terms of transition region pressures, the values that can be found in the literature (see, e.g., *Dere et al.*, 1982) are about $P_e = 1\text{x}10^{15}$ cm^{-3} K for the quiet sun.

Recently, many results based on SOHO have started to be published. The results obtained during this thesis work are described in Chapter 5. *Young and Mason* (1997) use O IV and Mg VII lines to estimate densities in bright transition regions. *Pinfield et al.* (1999) presents the first detection of an O V forbidden line and use it to deduce $N_e \simeq 10^{8.5}$ for the quiet sun. *Doschek et al.* (1998a) presents densities derived from the O V 759.441 and 761.128 Å lines observed at the limb by SUMER, and finds densities inside coronal holes ($N_e = 2 - 3\text{x}10^9$), a factor of two lower than in the quiet sun. No differentiation between cell-centres and network regions was possible, because the lines were observed at the limb in this case.

1.2.5 Element abundances

A large number of papers (and reviews, see above), have been written on this subject, and there are still differences of opinion on the reality and importance of the FIP effect. (Recall that different solar structures show different element abundances, and these appear to be related to the first ionization potential of the elements, with the low-FIP (≤ 10 eV) elements tending to have higher abundances. Articles that deal with solar abundance determinations and models include these by: *Mariska* (1980); *Veck and Parkinson* (1981); *Widing et al.* (1986); *Widing and Feldman* (1989, 1992, 1993); *Feldman and Widing* (1990, 1993); *Schmelz* (1993); *Laming et al.* (1995); *Geiss* (1995); *Schmelz et al.* (1996); *Fludra and Schmelz* (1995); *Grevesse and Anders* (1991); *Peter* (1998); *Grevesse and Sauval* (1998) and *Grevesse and Sauval* (1999). Photospheric abundances of most elements are relatively well determined (with uncertainties of the order of 15%), although values are continuously changing (see, e.g. the photospheric C, N, O abundances that in the recent study of *Grevesse and Sauval*, 1998, are about 20% lower than the previously quoted values). The photospheric abundances of the noble gases (as e.g. Ne and Ar) are not directly measured (because absorption lines of these elements are not present in the photospheric spectra). Their values are derived from carbonaceous meteorites, and therefore have large uncertainties.

The coronal values are still very uncertain, because they depend critically on the method of derivation. Most relative abundances have been measured in situ by various spacecraft studying the solar wind, or else with EUV spectroscopic techniques (which rely on the accuracy of the atomic physics). In general it has been found, from direct observations, that low-speed solar wind (SSW) and gradual Solar Energetic Particle events (SEP) show a permanent large scale FIP effect (of the order of 4-5), while in the high-speed solar wind (HSSW), no significant FIP-bias has been measured. This has also been confirmed by Ulysses observations of the Mg/O ratio (*Geiss*, 1995).

In almost all papers that derive element abundances using X-EUV spectroscopy, a large scatter of values is found. In some cases, for a few elements there are large deviations from the 'canonical' photospheric values. For example active regions show FIP effect factor from 0 to 4-5. Table 1.2 lists the most commonly used representative sets of 'standard' coronal and photospheric values, as used in this thesis.

The recent SOHO results have not solved the abundance problems, and if anything are creating more confusion on this subject. A critical review of the different EUV spectroscopic methods, with a re-analysis of Skylab data, is given in Chapter 2. It is found that crude approximations have been applied in many cases, and some important effects neglected, such as the presence of DEM distributions in the plasma. *Schmelz* (1993) is one of the few authors that apply a DEM method to X-ray spectra of solar flares to deduce relative element abundances, finding enhancements in the Ne/O and S/O abundance ratios, relative to their photospheric values.

Table 1.2: *Coronal (*Feldman *et al., 1992b) and photospheric (*Grevesse and Anders*, 1991) element abundances. Note that these photospheric abundances have been adopted as reference values throughout this thesis. The FIP values are from* Martin and Wiese *(1996).*

Z	Element	Coronal	Photospheric	FIP (eV)
1	H	12.0	12.00	13.59
2	He	10.9	10.90	24.59
6	C	8.59	8.60	11.26
7	N	8.0	8.00	14.53
8	O	8.89	8.93	13.62
9	F	-	4.56	17.42
10	Ne	8.08	8.09	21.56
11	Na	6.93	6.33	5.14
12	Mg	8.15	7.58	7.65
13	Al	7.04	6.47	5.99
14	Si	8.1	7.55	8.15
15	P	-	5.45	10.49
16	S	7.27	7.21	10.36
17	Cl	-	5.50	12.97
18	Ar	6.58	6.56	15.76
19	K	-	5.12	4.34
20	Ca	6.93	6.36	6.11
21	Sc	-	3.10	6.56
22	Ti	-	4.99	6.83
23	V	-	4.00	6.75
24	Cr	-	5.67	6.77
25	Mn	-	5.39	7.43
26	Fe	8.1	7.67	7.90
27	Co	-	4.92	7.88
28	Ni	6.84	6.25	7.64
29	Cu	-	4.21	7.73
30	Zn	-	4.60	9.39

Schmelz et al. (1996) report anomalous Ne/O abundance variations, by about a factor of two, both below and above the 'standard' coronal value of 0.15 for the relative abundance of these two high-FIP elements.

The Helium abundance is not reliably determined from X-EUV observations. In the HSSW and SSW the He abundance is very variable but on the average is 2-3 times lower than the photospheric value.

Coronal hole abundances have only been estimated by a few authors. In general, they do not show significant FIP effects. Coronal hole plumes are a special case, in the sense that large FIP biases have been reported (*Widing and Feldman*, 1992), from a single EUV observation close to the limb of the brightest polar plume observed by Skylab. Analysis of plume abundances should therefore be useful to test theoretical models that try to explain the FIP effect (see e.g. *Peter*, 1998).

Feldman and Widing (1993) found that Ne/Mg is lower in open field regions than in closed field regions, but there is a large scatter in the values they obtained. Assuming a Ne/Mg photospheric ratio of 3.39, and a constant pressure of 1.2 x $10^{15} cm^{-3} K$ in the transition region, and therefore a density of 3 x 10^9 for the selected ions, they found Ne/Mg values in the ranges 1.5-2 and 1.8-4.6 for the coronal holes and quiet regions respectively. *Habbal, Esser, and Arndt* (1993) used intensity ratios of three spectral lines from coronal hole images recorded by Skylab S-O55 on 1973 December 13, to derive O, Ne and Mg abundances. They found the values: A_b(O) = 8.96, A_b(Ne) = 8.2, and A_b(Mg) = 7.65 (on the usual log scale where A_b(H) = 12).

Very recently, some results from SOHO observations have been published.
Young and Mason (1997) have found large variations in Mg/Ne from CDS active region observations. *Feldman et al.* (1998) present SUMER off-limb observations which confirm a relative FIP effect of a factor of about 4 between a quiet sun streamer region and above the north coronal hole, assuming that the plasma was isothermal. However, it has to be pointed out that they used lines from different ions, and found that '*the Ne VIII, Na IX, Mg X lines, all of which belong to the Li-like isoelectronic sequence, appear to indicate a systematic lower effective FIP bias value than the rest of the lines*'. Since they used the O VI 1032 Å to normalize all the other lines, and since O VI *is* also of the same isoelectronic sequence, their result should be treated with caution. Examples of the particular behavior of the Li-like ions have also been found during the course of the present work, and these are presented later in this thesis. *Doschek et al.* (1998b) has also recently presented SUMER off-limb observations in the quiet sun (streamer) and polar coronal hole regions but they analysed lines of Si VII and Ne VII as representatives of low- and high-FIP elements. Surprisingly, they found photospheric values for Si/Ne (i.e. no FIP effect) in the streamer regions, and *an enhancement* of Si/Ne (i.e. 'anti-FIP' effect) in a coronal hole inter-plume region. However this last result was only a factor of 2, which is within the overall

uncertainty deriving from the atomic physics and the observational errors.

It would be useful to determine the individual elemental abundance values (relative to hydrogen), but these are difficult to measure in the corona. In principle, they can be determined by Solar Energetic Particle (SEP) measurements, or by spectroscopic measurements, by comparison of line intensities with either hydrogen continuum emission (which is always contaminated by some scattered background intensity), or with the resonantly scattered hydrogen emission lines observed in the corona. However, the errors in these methods mean there is some uncertainty as to whether the observed variations are in fact due to a depletion of high-FIP elements or an enhancement of low-FIP elements. This is a long-standing issue in solar physics. *Veck and Parkinson* (1981) were the first to compare line intensities and hydrogen continuum emission and found that the low-FIP elements seem to have their photospheric values, and that high-FIP elements are *depleted*. *Fludra and Schmelz* (1995) applied a DEM analysis on the same solar flare spectra examined by *Schmelz* (1993), combining the line information with hydrogen continuum data. They found high-FIP elements *depleted*, compared with their photospheric values, with a gradual FIP-effect. Direct measurements of inner-shell Fe lines have also shown (*Phillips et al.*, 1994, 1995) that the coronal Fe abundance is equal to the photospheric one, within a factor of two, and therefore if the FIP effect exist, it is a *depletion* of the high-FIP elements. Other papers (see, e.g., *Meyer*, 1993; *Reames*, 1995, from SEP analysis) point in the opposite direction, i.e. they found that low-FIP elements are *enhanced* in the corona, while high-FIP elements retain typically the photospheric abundances (and therefore are *not depleted*). More recently, *Raymond et al.* (1997) have used SOHO/UVCS data to determine absolute abundances in the high coronal streamer regions, from a comparison of emission lines and H I scattered light. They found that high-FIP elements are *depleted* even by factors of ten, in the core of an equatorial streamer (but with large spatial variations).

Regarding possible explanations for the observed FIP effect, it has been suggested (e.g. *Meyer*, 1993) that this depletion is occurring at the chromospheric level (T $\leq 10^4$ K) where the low-FIP elements are more easily ionized by electron collisions. In fact, the FIP effect implies an ion-neutral fractionation, and this can take place only at those temperatures, where the ions are only partially ionized. Then, in the presence of open magnetic field lines these ions can drift out into the corona to become more ionized. For closed magnetic structures, the ions would be trapped. Therefore, the abundances observed in the open field regions would reflect the production rates of the first ions at the coronal base, while those of the closed regions would be similar to the photospheric values. However, the recent SOHO data seem to introduce more questions, instead of solving the long-standing problems. For example, there have been independent indications (*Raymond et al.*, 1997, from

UVCS data; *Feldman et al.*, 1998, from SUMER observations) of gravitational settling, which makes ions of heavier elements behave differently from the other ones, thus casting doubt on the whole physical reason for the creation of the observed element abundance variations.

Another process that can affect element abundance variations is ambipolar diffusion (see *Mariska*, 1992, p. 184). In the lower transition region, the electrons are more mobile, because of the presence of a large number of neutral atoms. This will create an electric field and enhance the diffusion of the ions. This process is dependent on ionic charge, not on FIP.

1.2.6 Coronal plumes

Solar coronal plumes are common features and they originate in coronal holes. They appear as ray-like, extended (up to few solar radii) structures in white-light eclipse coronagraph images of the polar regions (see, e.g., *van de Hulst*, 1950; *Saito*, 1965), and as shorter spikes in EUV images (e.g. *Ahmad and Withbroe*, 1977; *Widing and Feldman*, 1992; *Walker et al.*, 1993), at X-rays (*Ahmad and Webb*, 1978), and possibly also at radio wavelengths (*Gopalswamy et al.*, 1992). It is important to study plumes because they are the only stable observable structures within coronal holes, where the heating and acceleration processes lead to the formation of the fast solar wind (FSW).

In EUV, plumes have been known to be visible only in emission lines that form over a narrow range of temperatures (e.g. *Widing and Feldman*, 1992), with emission from ions that form at temperatures above a million degree almost absent.

DeForest et al. (1997) showed that plumes seen in white light and in the EUV are the same physical objects, tracing plume structures from the lower corona up to 15 $R_\odot$. Plumes have been shown to diverge super-radially, with an expansion factor ~ 10 (*DeForest et al.*, 1997 and references therein). They are stable structures, lasting from a few hours to more than one day, and tend to be recurrent, i.e. appear and disappear at the same locations (*Lamy et al.*, 1997). They are usually rooted in the boundaries of chromospheric cells (see, e.g., *Wang and Sheeley*, 1995b; *DeForest et al.*, 1997), where there is a concentration of unipolar flux of the same sign as that of the ambient coronal hole. In many cases a small concentration of opposite magnetic flux is found at these sites, (*Wang et al.*, 1997), suggesting that magnetic reconnection plays an important role in the formation and evolution of plumes (*Wang*, 1998). On the other hand, not all magnetic flux concentrations on network junctions inside coronal holes have plumes associated with them.

Because of their morphology, it is generally assumed that plumes trace the open field lines of the coronal holes. They would therefore be expected to exist in low-latitude coronal holes as well as in polar holes. A few such observation have been claimed (*Wang and Sheeley*, 1995a; *Woo*, 1996). *Del Zanna and Bromage* (1999a) - see Chapter 5 in this thesis - report the first detection by SOHO of a low latitude plume visible on the disc.

These features are also particularly interesting because they present an extreme case of particular element abundances, as explained above.

Prior to SOHO, it was not possible to clearly distinguish characteristics of plumes and ambient coronal hole (inter-plume) regions. Density and temperature measurements were mostly based on Skylab and coronagraph data, and were only very approximate determinations. Densities were usually estimated from the plume brightness in Thomson scattered white light coronagraph observations, applying the *van de Hulst* (1950) technique. For example, *Fisher and Guhathakurta* (1995) presented densities of polar coronal holes and plumes extending from 1.16 to 5 $R_\odot$, as a function of the radial distance. They showed that plumes have shallower density gradients, and need to be 3-5 times denser than their surroundings, in order to explain these white light coronagraph observations. Temperatures were usually only estimated from intensity gradients of EUV emission lines, assuming hydrostatic equilibrium and ionization equilibrium, which were shown to be reasonable approximations (*Widing and Feldman*, 1992).

In the reminder of this Section, the main observational results are re-evaluated (in chronological order), followed by comments on the theoretical models used to interpret them.

pre-SOHO observations.

Saito (1965) presents white-light observations of plumes. With the assumptions that plumes are isothermal and in hydrostatic equilibrium a temperature of 1.2x10^6 K was found.

Ahmad and Withbroe (1977) presented Skylab observations of three off-limb polar plumes seen with the HCO instrument. Intensity profiles across the observed plumes, at a fixed radial distance from the Sun, suggest that the density distribution across them can be represented by a gaussian profile. Also, the intensity ratios of Mg X/O VI lines show a marked decrease in the plumes (with constant values inside them), suggesting that plumes contain cooler material than their surroundings and have a constant temperature across their width. Radial profiles of the Mg X/O VI intensity ratio along the plumes, in the range 1.03-1.11 $R_\odot$, show a tendency to increase from 0.3 to about 0.8. Assuming a relative Mg/O abundance of 0.079, these authors derived the associated isothermal temperature increase, with values $T \simeq 1.1$x10^6 K. A calculation was performed by the author using more recent atomic data (CHIANTI), assuming that only the transitions Mg X 624.941 and O VI 1031.91 contributed to the observed lines, gives a different range of temperatures (T = 8.3x10^5 ,9.3x10^5K), for a Mg/O abundance of 0.079. In fact, much of the uncertainty in the derived temperature is in the relative abundance. The Mg/O abundance that *Ahmad and Withbroe* (1977) adopted is quite high, compared with 0.045 for photospheric (*Grevesse and Anders*, 1991), or 0.18 for coronal abundances (*Feldman et al.*, 1992b). Assuming a photospheric abundance, for example, increases the temperatures T = 8.9x10^5 to 1.15 x10^6 K. Thus, the plume temperatures deduced from *Ahmad and Withbroe* (1977) were probably overestimated. The density along the plumes was estimated from the temperature profiles and so, given the large uncertainties in the derivation of the temperature, their density estimates should be treated with caution.

Ahmad and Webb (1978) presented Skylab S-054 X-ray images of polar plumes seen off-limb. Following *Ahmad and Withbroe* (1977), they assume a gaussian shape for the density distribution. Using some assumptions (e.g. that plumes are isothermal along the line of sight), they deduce radial profiles of the electron pressure, between 1.04 and 1.1 $R_\odot$. These curves are well fitted with a model that assumes hydrostatic equilibrium and an isothermal temperature along the plumes of 7.9x10^5 K. They then reject the model because this temperature is too low compared to those derived by *Saito* (1965) and *Ahmad and Withbroe* (1977).

Walker et al. (1993) analysed some plume X-ray images obtained by multi-layer optics. Compared to Skylab observations, these have better spatial resolution ($\sim 1.5''$), and extend up to 0.6 $R_\odot$ off the limb. They could only estimate plume temperatures and densities from the scale height of the intensity in one filter image, together with the application of a model which assumed that plumes have higher densities and slightly higher temperatures than the inter-plume regions. Hence, their deduced temperature and densities are very approximate.

Widing and Feldman (1992) analysed the brightest polar plume observed by the Skylab S082-A spectroheliograph at the limb, on 1973 December 11. They measure the intensities at plume centre of various lines (Ne VI, VII, Mg VI-VIII, Na VIII, Ca IX,X), at different heights above the limb. They derived a hydrostatic temperature for each ion, assuming hydrostatic equilibrium to relate temperature and density, and relating the measured intensities with the density. They found good agreement between this temperature and the temperature of maximum emission in ionization equilibrium. This agreement suggests that the plume could be approximated by a multi-thermal structure, with each ion emitting under hydrostatic and ionization equilibrium conditions. Outflow velocities in the range 10-20 km s^{-1} were consistent with their data. The electron density derived from the Mg

VIII [436.7/430.5] ratio has a large scatter around $N_e = 10^9 cm^{-3}$ and does not show the decline toward higher altitudes that is derived from the intensity measurements. A comparison of this mean value with the average density derived from the Mg VIII EM suggests a 0.3 filling factor for that plume. Finally, *Widing and Feldman* (1992) performed an average line differential emission measure (DEM_L) analysis (see Chapter 2, below for a definition), using the line intensities as measured at two heights. This analysis was used to derive relative element abundances, and it represents the only one made on plumes. Their result is that this plume had an Ne/Mg abundance ratio 10 times smaller than the photospheric ratios, thus this plume showed an FIP effect of 10. *Widing and Feldman* (1992) also found that the Ca/Mg and the Na/Mg ratio do not differ by more than a factor of 2 from the corresponding photospheric values.

Wang and Sheeley (1995a) have identified in the Skylab S082-A EUV images some plume-like features inside low-latitude coronal holes undergoing either east or west limb passage. Like the polar plumes, these diffuse structures are prominent in the Mg IX (368 Å) images and rarely visible in the Ne VII (465 Å) images, probably because of the lower temperature of formation of Ne VII and the reduced Ne/Mg abundance ratio in the plumes. Also, at the base of the plumes, compact network enhancements (within the weak background emission of the coronal hole) are visible in the Ne VII, He II (465, 304 Å), and sometimes other coronal lines. A plume was observed during its movement inward from the limb; its lifetime was more than one day but less than two; the associated hot emission (Fe XV 284 Å) near the base remained strong for more than 11 hours, and began to fade after 22 hours. Although these authors only present a few cases, it could be concluded that coronal plumes with similar characteristics can occur in regions of open magnetic field lines at *any* latitude, from polar regions to equatorial ones.

Wang and Sheeley (1995b) use a theoretical model to show how the appearance of coronal plumes varies, depending on their orientation relative to the line of sight. In their model, plumes are aligned along open magnetic field lines, which are calculated using a potential field method. Hydrostatic equilibrium is also assumed. The simulations show that plumes would appear as diffuse objects when viewed projected on the disc. With the aid of this simulation, those authors identified various plumes at different latitudes in a coronal hole seen , in Mg IX (368 Å) spectroheliograms from Skylab S082-A, and also located underlying network features in the corresponding Ne VII (465 Å) and He II (304 Å) images. When the base of the plumes was visible (in Mg IX) against the disc, intense network features within their base areas were always found, but the converse did not hold: not every Ne VII or He II bright point had an associated Mg IX plume. An analysis of a lower latitude hole, observed on 1974 January 15, compared with a simultaneous high-resolution magnetogram, showed that the plumes occurred in the vicinity of mixed magnetic polarity regions, although not every magnetic bipole had a plume associated with it. Mixed polarity was present wherever neon and helium enhancements occurred in the coronal hole.

Woo (1996) reported the detection of low-latitude plumes using Ulysses radio ranging observations. *Fisher and Guhathakurta* (1995) estimated densities of south and north polar coronal holes and rays extending from 1.16 to 5 $R_\odot$, as a function of the radial distance. The densities were derived by applying the van de Hulst technique to the 1993 April 11-12 observations obtained with the white-light coronagraph aboard the Spartan 201-01 spacecraft, together with the ground-based K-coronameter on Mauna Loa, Hawaii. Coronal rays appeared as coherent structures at much higher altitudes (5 $R_\odot$) than previously observed.

Theoretical models.

Since the high-speed solar wind originates from open field regions, a full solar wind theory should also explain the observed properties of coronal plumes. Various solar wind-plume models have been proposed (see *Wang*, 1994, *Velli et al.*, 1994 and *Del Zanna*, 1997, for some of the most recent ones) but they all suffer from a lack of observational constraints, in particular on the temperature of the plumes.

Wang (1994) developed a model of steady and radial mass flow of a single-fluid within a polar plume, exemplified as a flux tube with constant section. A two-component heating source in the energy conservation equation was assumed. In addition to the "global" heating (with damping length H_m $\sim R_\odot$), required to drive the high-speed wind from the plume and inter-plume regions, the model showed that a large amount of energy must be dissipated over a scale $H_b \ll R_\odot$, in order to produce the high plasma densities observed in the plumes ($N_e \geq 10^9$ cm^{-3}). This concentrated heating gives rise to a steep temperature gradient with a local temperature maximum just above the plume base, while at greater distances the plume is cooler than the inter-plume regions. Although the mass flux densities are higher within the plumes, the inter-plume regions occupy most of the polar hole area and are therefore the main source of the high-speed polar wind.

Velli et al. (1994) presented a solar wind model which takes into account the possible origin of fast solar wind streams in coronal plumes. They model the solar wind as a combination of warm, dense plumes immersed in a cooler and less dense solar wind. Their model shows plumes expanding beyond 10 $R_\odot$ and having larger β than the inter-plume regions. *Del Zanna* (1997) solved a self-consistent ideal 2-D MHD steady model that took into account pressure, inertial and gravity forces, under the assumptions of azimuthal symmetry around the plume axis and constant temperature along the field lines in a low-beta plasma. This model reproduces basic plume features such as the super-radial expansion near the plume base.

SOHO observations

Many problems concerning coronal plumes were therefore unsolved at the time of SOHO's launch. For example, it was not entirely clear whether plumes were cooler or hotter than their surroundings, nor whether plumes are not the source of the high speed solar wind. The results for element abundances suggest that plumes are not the source of the high speed solar wind.

SOHO spectroscopic observations have sufficient spatial and spectral resolution to allow a more accurate characterisation of plumes than was previously possible. Some recent results are summarised here.

Wilhelm et al. (1998) presented SOHO SUMER off-limb (in the range 1.03 - 1.6 $R_{\odot}$) spectroscopic observations of plume and inter-plume regions. They estimated temperatures and densities using Mg IX and Si VIII line ratios. Plume temperatures are approximately constant around $T = 780\ 000$ K and then decrease at higher radial distances, while inter-plume temperatures were found to increase over the same height range. Densities of both plume and inter-plume regions start at $N_e \simeq 1\text{x}10^8$ cm^{-3} and then decrease with height, with plumes having shallower gradients.

Although these adopted line ratio techniques are among the most accurate for determining temperatures and densities from EUV spectra, the *Wilhelm et al.* (1998) results are severely limited by the fact that plumes and inter-plume regions were compared using data over a time span of six months, and at different spatial locations.

SUMER (e.g., *Hassler*, 1997) and UVCS (*Noci et al.*, 1997, *Kohl et al.*, 1997) off-limb observations have shown that the spectral line widths in the inter-plume lanes are larger than in the plumes, indicating lower temperatures in plumes as a possible explanation.

EIT images were used by *DeForest et al.* (1997) to estimate plume temperatures in the range $1 - 1.5\text{x}10^6$ K, finding higher temperatures in the inter-plume lanes (but by no more than 30%).

The new SOHO results therefore all suggest that plumes are slightly cooler and denser, and that the high-speed wind is likely to stream out of the inter-plume regions. In this thesis (Chapters 5 and 6) new results obtained from CDS observations are presented, confirming these early SOHO findings.